A $(Bi_2O_2)^{2+}$ layer as a significant carrier generator and transmission channel in $CaBi_2Nb_2O_9$ platelets for enhanced piezo-photo-catalytic performance

Qiong Liu[1], Faqi Zhan[2], Xiaogang Luo[1], Qiuyan Yi[1], Zhida Xiao[1], Di Zhai[1], Jingxiang Huang[1], Yan Zhang[1], Hang Luo[1]*, Dou Zhang[1]*, Chris R. Bowen[3]

[1] State Key Laboratory of Powder Metallurgy, Central South University, Changsha, Hunan 410083, China.

[2] State Key Laboratory of Advanced Processing and Recycling of Non-Ferrous Metals, Lanzhou University of Technology, Lanzhou 730050, Gansu, China.

[3] Department of Mechanical Engineering, University of Bath, Bath BA2 7AK, UK

*Corresponding author

E-mail address: hangluo@csu.edu.cn (Hang Luo)

E-mail address: dzhang@csu.edu.cn (Dou Zhang)

Abstract

The low photocatalytic conversion efficiency, poor light absorption and high charge recombination rate of traditional semiconductor photocatalysts continues to be a significant research challenge. In this paper, by combining detailed experimental and modelling techniques, we report on the unique potential of $CaBi_2Nb_2O_9$ (CBN) platelets that can couple both piezo- and photo- multi-field effects to overcome these issues and realize high-efficiency hydrogen production and dye degradation. The surface adsorption of OH^- and dye molecules is improved as a result of the built-in electric field, thereby demonstrating an enhanced piezo- and photo-catalytic H_2 production activity, with a high rate of 96.83 $\mu mol \bullet g^{-1} \bullet h^{-1}$. The piezo-photocatalytic decomposition ratio for 100 mL RhB dye of 10 mg/L can reach up to 98.7% in 32 min using only 0.05 mg of CBN platelets (k = 0.131 min^{-1}). It is shown that the careful introduction of regularly arranged layers of $(Bi_2O_2)^{2+}$ into the CBN platelet structure provides a high transport of photoelectrons via a pathway of $(Bi_2O_2)^{2+} \rightarrow (CaNb_2O_7)^{2-} \rightarrow$ CBN surface. The electron density distribution of Bi atoms is also found to be enriched on the facets of (020) and (200) crystal planes in the CBN platelets, which is beneficial to the oxidation reduction reaction. Furthermore, the large deformation of CBN platelet during the application of ultrasound leads to an increase of the piezo-induced built-in electric field to improve charge separation and migration. This work therefore provides a new perspective in the design and manufacture of advanced materials with enhanced piezo- and photo-catalytic performance by exploiting multi-field coupling effects.

Keywords: $CaBi_2Nb_2O_9$; Piezo-photocatalysis; Multi-field coupling effects; DFT

1. Introduction

A variety of energy harvesting techniques have been studied in recent decades to relieve the increasingly prominent energy crisis and ongoing environmental pollution challenges [1, 2]. As a result, there has been a growth in research that explores the potential of coupling multiple effects, such as photo-, magneto-, piezo-, and pyro-effects in catalytic applications [3]. For example, multi-field coupled catalytic materials have been applied in hydrogen production [4-8], pollutant degradation [9-12], anti-cancer biotherapy [13-15], sterilization [16-18], disinfection [19, 20], and carbon dioxide reduction [21, 22].

The coupling of both piezoelectric and photoelectric effects has been widely studied and recently been shown to exhibit enhanced performance [23-25]. There are two primary approaches to achieving piezo- and photo-electric coupling. Firstly, the material itself can demonstrate both effects to provide an *intrinsic* multi-field response. Secondly, it is possible to use physical or chemical synthesis to combine two or more materials that each exhibit a specific response to create a *composite* multi-field material. When compared with the more commonly explored composite materials, materials with an intrinsic multiple field effect generally exhibit a weaker coupling coefficient, but have the advantages of low cost, simple operation, and therefore future development potential.

Recently, the $[Bi_2O_2]$-based layered two-dimensional (2D) materials, such as BiOCl [26], $PbBi_3O_4X_3$ (X = Cl, Br) [27], $Bi_4Ti_3O_{12}$ [28] and Bi_2O_2S [29], have shown intriguing performance in terms of their electronic, optoelectronics,

piezoelectric and photocatalytic applications. The layered structure of these materials provides advantages in catalytic applications, which include providing sufficient space for polarized orbitals and atoms, and being conducive to the formation of a self-built electric field to provide effective separation of electron-hole pairs [30]. The material $CaBi_2Nb_2O_9$ (CBN) is a form of Aurivillius-type photocatalysts and has been explored for photocatalytic water splitting [31]. However, CBN has a wide band gap of 3.4 eV and can only absorb visible light below 360 nm, which greatly limits its catalytic performance [32]. Interestingly, CBN is a typical bismuth layered structure compound, and due to its layered perovskite structure, CBN has the characteristics of a strong spontaneous polarization, large anisotropy of piezoelectric and dielectric properties, temperature stability, and high mechanical quality factor, thereby demonstrating significant potential in multi-field coupling for catalytic enhancement. The spontaneous polarization in perovskite structured CBN piezoelectric ceramics is primarily due to the displacement of the B-site ions along the c-axis direction, resulting in the misalignment of positive and negative charge centers in the unit cell. The internal electric field of $[Bi_2O_2]$-based layered materials along the [001] direction has the potential to favor charge separation in photocatalytic reactions, thereby improving overall photocatalytic performance.

In this work, two $CaBi_2Nb_2O_9$ (CBN) morphologies, namely CBN particles and CBN platelets, were synthesized by the solid phase method and molten salt method, respectively, and applied to the catalytic degradation of dyes and splitting water for hydrogen production. To allow the intrinsic influence of the CBN morphology on

catalytic performance to be explored, an in-depth analysis of the materials included phase analysis, electron microscopy, UV-Vis spectroscopy, and catalytic performance, which was combined with Density Functional Theory (DFT) analysis and multi-physics modeling. As a result, we demonstrate that the electron density distribution of Bi atoms on the facets of (020) and (200) crystal planes in the CBN platelets is stronger than that on the facets of (113) and (022) crystal planes in CBN particles, which is beneficial to the platelets exhibiting an enhanced oxidation reduction reaction. The introduction of regularly arranged layers of $(Bi_2O_2)^{2+}$ in the CBN platelet also provides high transport of photoelectrons via a pathway of $(Bi_2O_2)^{2+} \rightarrow (CaNb_2O_7)^{2-} \rightarrow$ CBN surface. Furthermore, a strong deformation of CBN platelets under the application of ultrasound leads to an increase in piezo-induced built-in electric field, which leads to an improvement the charge separation/migration. As a result, the CBN platelets exhibits a superior piezo-photocatalytic performance compared to the CBN particles. This work therefore provides new insights in the design of new advanced materials with enhanced catalytic performance by judicious coupling of both piezo- and photo-catalytic effects.

2. Experimental Section

2.1. Reagents

$CaCO_3$ (99.99%, Sinopharm Chemical Reagent Co), Nb_2O_5 (99.5%, Sinopharm Chemical Reagent Co., Ltd.) and Bi_2O_3 (99.99%, Macklin) were used as raw materials. NaCl (99 %, Sinopharm Chemical Reagent Co., Ltd.) and KCl (99.8 %, Sinopharm Chemical Reagent Co., Ltd.) were used as the molten salt.

2.2 Preparation of $CaBi_2Nb_2O_9$ (CBN) particles

A conventional solid-state sintering approach was applied to the synthesis of the CBN particles. The raw materials were weighed according to the chemical ratio and mixed in ethanol and zirconia grinding media with a ball mill in a mass ratio of 1:3, for 12 h with a speed of 300 r/min. The dried mixtures were calcined at 925 °C for 2 h and then milled again under the same conditions for 24 h. The CBN particles are indicated as “CBN-PA” in this work.

2.3 Preparation of $CaBi_2Nb_2O_9$ (CBN) platelets

The raw materials were mixed according to their stoichiometric compositions. NaCl (99 %) and KCl (99.8 %) salts in a mass ratio of 1:1 were added as the molten salt, and the mass ratio of CBN to the molten salt was 1:1. All powders were mixed in ethanol and milled for 24 h with a speed of 300 r/min. The dried powders were calcined at 950 °C for 6 h, and then washed with deionized water to remove the NaCl and KCl. Finally, the CBN platelets were dried. The CBN platelets are termed “CBN-PL” in this work.

2.4 Characterization

An X-ray diffractometer (XRD, D/Max 2250, λ=1.5418 Å, PANalytical Empyren, Netherlands) was used to characterize the phase structure of the CBN particles and CBN platelets. The morphologies and nanostructures of the samples were verified by scanning electron microscopy (SEM, Oxford x-max 20, Tescan Mira3). A spectrophotometer (PGeneral TU-1901) was used to characterize the UV-Vis spectra of the samples, and the UV-vis spectrophotometer (UV-2600i, Island ferry, Japan) was

used to verify the diffuse reflection properties of dyes during catalytic performance testing. An electrochemical workstation (Chenhua CHI604E, Shanghai) was employed to characterize the photoelectrochemical (PEC) performances with a typical three-electrode configuration; a detailed test procedure is provided in the supporting information. The specific surface area of the particles and platelets were carried out with a particle size analyzer (Quantachrome QuadraWin). A Xenon lamp (300 W, PLS-SXE300D, Beijing Perfectlight) served as the source of optical drive and an ultrasonic machine (200 W, 45/80/100 kHz, KD-200, China) served as periodic mechanical strain drive. Piezo-response force microscopy (PFM, Bruker Multimode8) was employed to characterize the piezo-response of the particles and platelets.

2.5 Evaluation of catalytic performance

The piezo-, photo- and piezo-photocatalytic behavior for dye degradation was measured using a mass of 0.05 g of CBN for 100 mL RhB dye of 10 mg/L, and hydrogen production was measured using 0.05 g of CBN for 50 mL of deionized (DI) water with a Xenon lamp (300 W, PLS-SXE300E, Beijing Perfect Light) and/or ultrasonic machine (200 W, 45/80/100 kHz, KD-200, China), respectively. The degradation efficiency (C / C_0 × 100%) was quantitatively determined by the spectral ratio at the maximum absorbance; where C_0 is the initial concentration and C is the in-progress concentration at a reaction time of t. The piezocatalytic degradation reaction is in accordance with the pseudo-first-order kinetic equation of ln (C_0 / C) = k × t, where k is the rate constant.

3. Results and Discussion

3.1. Catalyst Characterization

The crystalline structure of the CBN particles and CBN platelets are analyzed with transmission electron microscopy (TEM) in Fig. 1. Both TEM and high-resolution TEM (HRTEM) analysis performed on a single CBN particle is presented in Figs. 1a and 1b, respectively. The granular structure of the particle is seen in Fig. 1a, with a regular structure of the planes seen in Fig. 1b. The interplanar *d*-spacing of 0.266 and 0.350 nm matches well with the interplanar spacing of the (022) and (113) in the CBN particle, respectively. Fig. 1c shows the corresponding selected area electron diffraction (SAED) pattern, which further confirmes the crystal plane structure of the CBN particle.

In Figs. 1d-1f, the distinct flake-like structure of the CBN platelets can be observed, where the ordered lattice fringes with interplanar *d*-spacing of 0.273 and 0.275 nm match the (020) and (200) interplanar of the CBN platelet, respectively. It has been reported that the chloride ion in the molten salt, which is based on KCl and NaCl, tends to be absorbed by Bi^{3+} in $(Bi_2O_2)^{2+}$ during melting and thus reduces the surface activation in the [001] direction; this results in an advantageous growth of the [100] and [010] directions [33]. The corresponding indexed fast Fourier transform (FFT) patterns of the CBN platelets are shown in Fig. 1f, which indicates the occurrence of a single-crystalline structure and that the zone axis is parallel to the z-axis of the layered structure of the CBN platelet. The surface of CBN platelet is parallel to the $(Bi_2O_2)^{2+}$ layered structure and the overall CBN platelet exhibits a regular structure, which is different to the CBN particle. The High-Angle Annular Dark Field (HAADF) and

elemental mapping images of the CBN platelet, shown in Figs. 1g-1k, indicate the distribution of each element in CBN platelet.

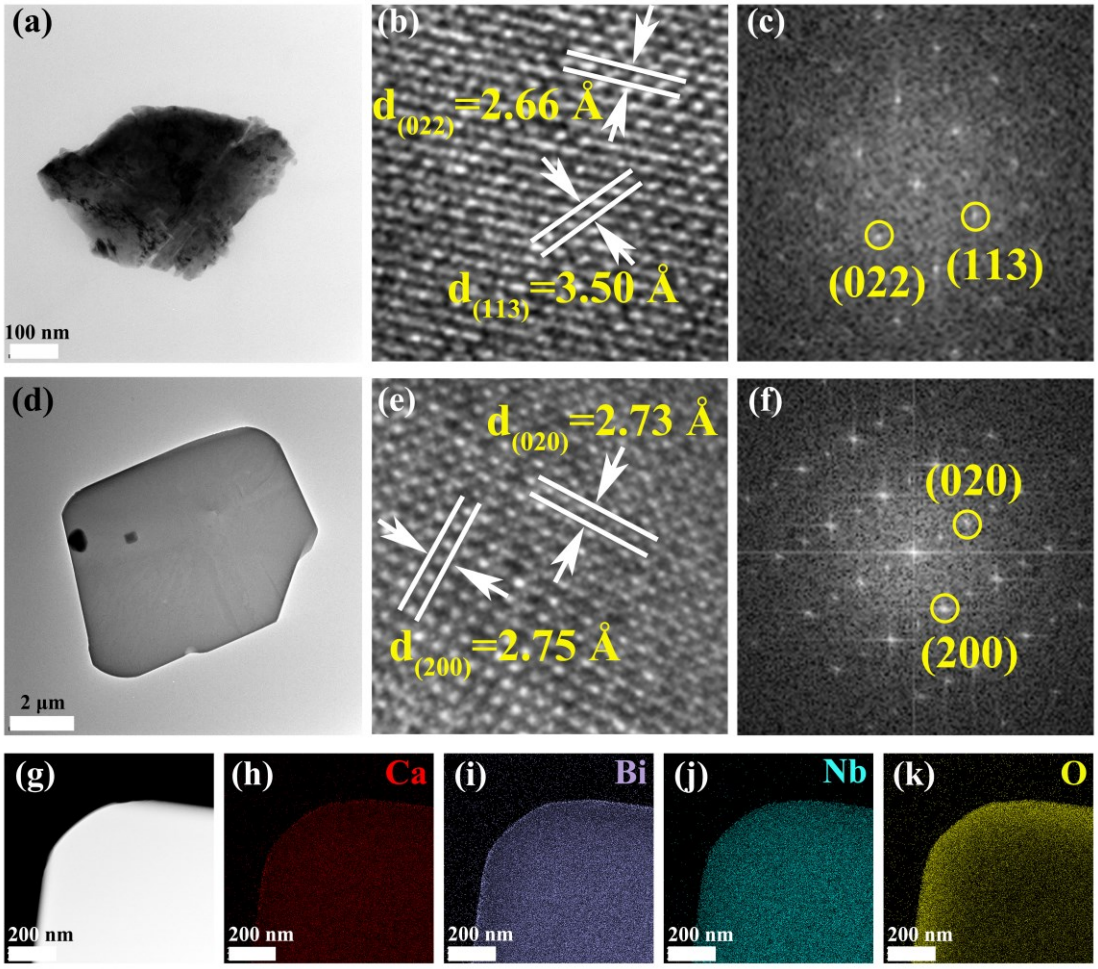

Fig. 1. (a) TEM, (b) HRTEM and (c) SAED images of $CaBi_2Nb_2O_9$ (CBN) particle; (d) TEM (e) HRTEM and (f) SAED images of CBN platelet. (g) HAADF images of CBN platelet and corresponding elemental mapping of (h) Ca, (i) Bi, (j) Nb and (k) O.

DFT calculations are further employed to better understand the differences between the different crystal planes of CBN. Figs. 2a and 2e show the atomic structure diagrams of (022) and (113) crystal planes of the CBN particles, and Figs. 2i and 2m are the atomic structure diagrams of (020) and (200) crystal planes of the CBN platelets, respectively. In Figs. 2b, 2f, 2j and 2n, the calculated electron density

distribution shows that the electron distribution of Bi atoms (the yellow atoms) exist in the (020) and (200) crystal planes, but are not present in (022) and (113) crystal planes at a total electron density distribution at the isosurface value of 0.5 $eÅ^{-3}$. This indicates that the $(Bi_2O_2)^{2+}$ layer is aligned along the [001] axis in the CBN platelets, which can allow more electrons to participate in the catalytic reactions, thereby facilitating catalytic performance. The electrostatic field derived from the layered structure and the dominating active exposing facets of the CBN platelets are also beneficial for the separation of charge carriers [30].

The highest occupied molecular orbital (HOMO) and the lowest unoccupied molecular orbital (LUMO) distributions of the (022) (Figs. 2c-2d) and (113) (Figs. 2e-2h) crystal planes of the CBN particles and the (020) (Figs. 2k-2l) and (200) (Figs. 2o-2p) crystal planes of CBN platelets are used to determine the reaction mechanism. It can be seen that the electron cloud of the HOMO and LUMO of these four crystal planes have a spatial distribution. This orbital distribution can effectively promote the separation of electron-hole pairs and generate a large number of active species, which is beneficial to the catalytic properties and potential decomposition of pollutants. Furthermore, in Fig. 2o, the oxygen atoms in $(Bi_2O_2)^{2+}$ layer with well-distributed orbitals can be used as electron transport channels between HOMO and LUMO, which further verifies that the $(Bi_2O_2)^{2+}$ layer is conducive to electrons transport and separation.

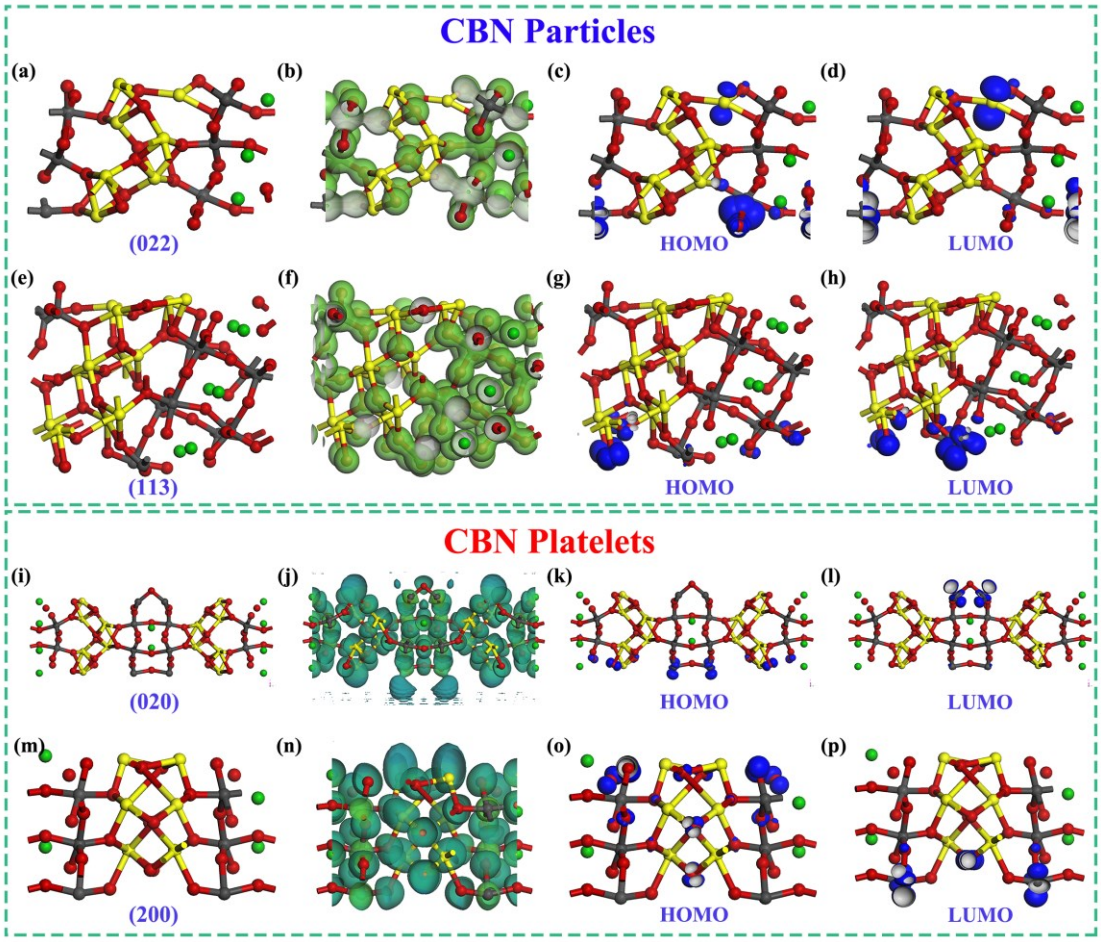

Fig. 2. (a) Atomic structure diagrams, (b) isosurface total electron density distribution of atoms (the atoms in yellow, red and gray represent Bi, O and Nb, respectively. The green areas represent the total electron density distribution at the isosurface value of 0.5 eÅ^{-3}.), (c) HOMO and (d) LUMO orbitals of (022) crystal plane in $CaBi_2Nb_2O_9$ (CBN) particles; (e)-(h), (i)-(l) and (m)-(p) are the same spectrums with (a)-(d) but for (113) crystal plane in CBN particles, (020) and (200) crystal planes in CBN platelets, respectively.

The work function of the top and bottom surfaces calculated from the (022) (Fig. 3a), and (113) (Fig. 3d) crystal planes of CBN particles, and the (020) crystal plane of the CBN platelets (Fig. 3g) are 4.193 eV and 4.818 eV, 3.495 eV and 5.625 eV, and 3.910 eV and 3.506 eV, respectively. The work function calculated from the energy

spacing between the vacuum level and Fermi level of the (200) crystal plane of the CBN platelets is determined to be 3.746 eV (Fig. 3j) in the potential energy curve. Combining the work functions of the top and bottom surfaces, the work function of the (020) and (200) crystal planes of the CBN platelets is lower than that of the (022) and (113) crystal planes of the CBN particles, thereby indicating that less energy is required for electrons to transition from the valence band to the conduction band in the CBN platelets; this can enhance the catalytic performance of the platelets due to the more easily excited electrons.

The total density of states (DOS) and partial density of states (PDOS) are further examined to explore the activation mechanism of electrons. The four crystal planes are calculated, as shown in Figs. 3b-3c, Figs. 3e-3f, 3h-3i and 3k-3l for the (022) and (113) crystal planes of the CBN particles and the (020) and (200) crystal planes of the CBN platelets, respectively. It can be seen that the valence band of the (020) and (200) crystal planes is much closer to the Fermi level, compared with the (022) and (113) crystal planes, which means that electrons are more easily excited since the valence band is electron-donating [34]. For all the crystal planes, the total density of states at the valence band arises from the O 2p, Bi 6p and Nb 4d orbital electrons, and the contribution of the O 2p orbital electrons is much higher than that of Bi 6p and Nb 4d [32]. The conduction band primarily consists of the Nb 4d, Bi 6p, Bi 4d and O 2p orbital electrons, and Nb 4d orbital electrons make the largest contributions. Therefore, the generated electrons accumulate in the $(CaNb_2O_7)^{2-}$ layer to generate $\bullet O_2^-$ radicals, while the holes will move towards the $(Bi_2O_2)^{2+}$ layer and subsequently react with

OH^- or H_2O to generate •OH radicals.

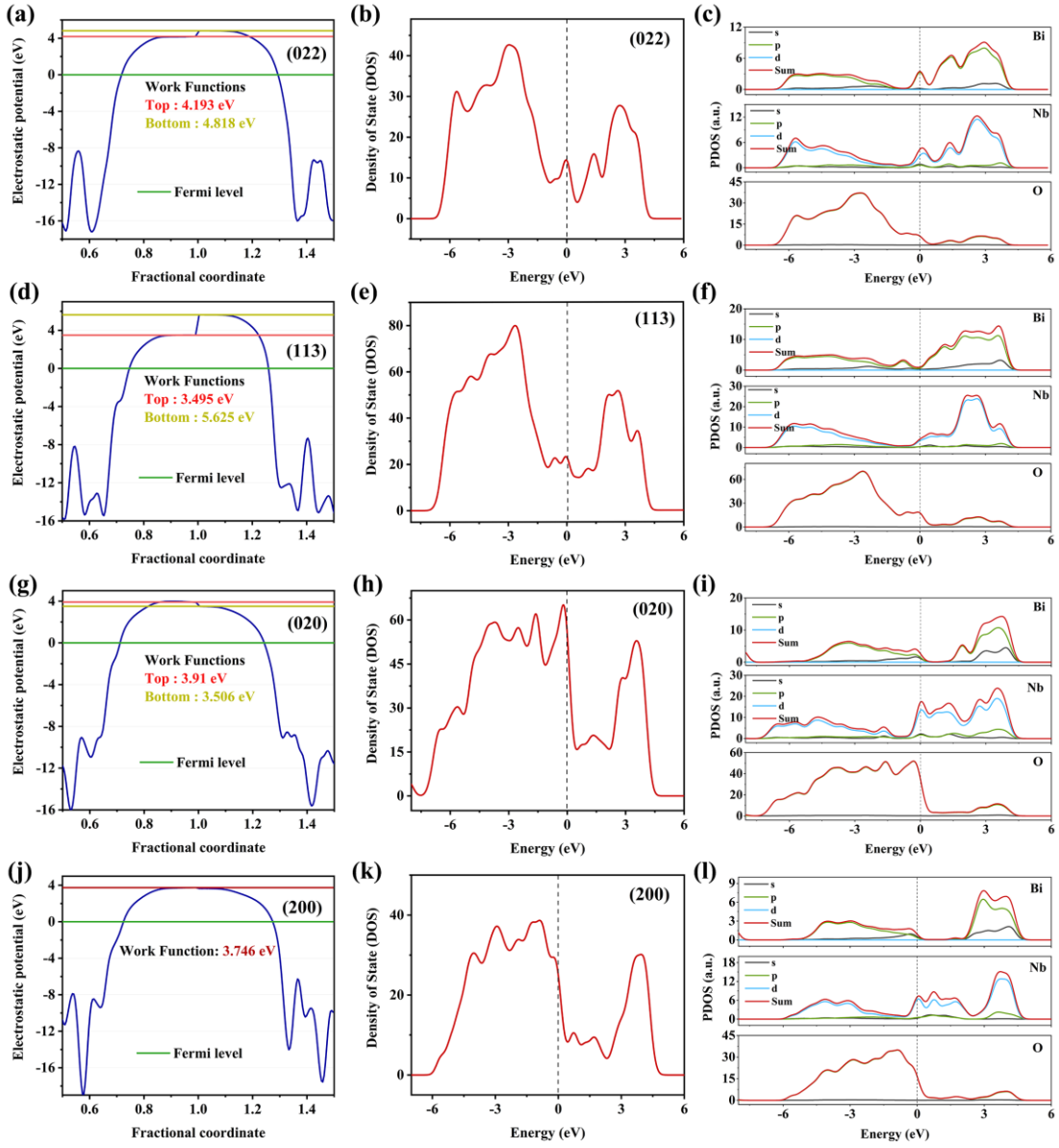

Fig. 3. (a) Calculated work function, (b) total density of state (DOS) and (c) partial density of states (PDOS) of the (022) crystal plane of $CaBi_2Nb_2O_9$ (CBN) particles; (d)-(f), (g)-(i) and (j)-(l) are the same spectrums as (a)-(c) for the (113) crystal plane of CBN particles, (020) and (200) crystal planes in CBN platelets, respectively.

The optical absorption characteristics of both the CBN particle and CBN platelet based catalysts are investigated by UV-vis diffuse reflectance spectra (DRS) analysis.

As seen by the insert figure in Fig. 4a, the CBN particles and CBN platelets exhibit inherent visible light absorption and the absorption edges are approximately 420 and 465 nm, respectively; this indicates that the CBN platelets have a wider range of visible light absorption compared with CBN particles. The band gap energies (E_g) are shown in Fig. 4a, and were determined by the Kubelka-Munk method according to the equation:

$$Ahv = B(hv-E_g)^{1/2} \quad (3)$$

The E_g of the CBN particles and CBN platelets are 3.10 and 3.03 eV, respectively [35]. The lower band gap of the CBN platelets indicate that less energy is required for electronic excitation from the valence band to the conduction band, which is consistent with the calculated work function. The energy band position of semiconductor materials is closely related to their potential application according to the kinetic barrier analysis; where potential applications include decomposition of water to produce hydrogen, reduction of carbon dioxide, and degradation of organic pollutions. As a result, a Mott-Schottky measurements were conducted to verify the position of the flat band potential. Both the CBN particles and CBN platelets are n-type semiconductors with positive slopes at different frequency, as represented in Figs. 4b and 4c. The flat band potential of the CBN particles and CBN platelets are 0.05 eV and 0.12 eV, respectively. Electrochemical impedance spectroscopy (EIS) for both the CBN particles and CBN platelets at 0.6 V vs. RHE in the presence of SO_4^{2-} is shown in in Fig. 4d. All EIS plots consist of a single semicircle, where the response from the CBN particles exhibits a smaller radius compared with the CBN platelets,

indicating a smaller resistance to charge transfer for the CBN particle. From the impedance spectra, the response at low frequencies corresponds to the bound diffusion of ions in the material. While the properties of the bound diffusion impedance are expected to essentially depend on the diffusion geometry, the diffusion length distribution in the materials are configurational [36]. During the electrochemical test procedure, although there is the same level of powder coating in the thin film, some stacking of CBN platelets is inevitable, which leads to an increase in interface transmission resistance. In addition, the lower specific surface area of the CBN platelets, compared to the CBN particles, leads to a reduced contact area between platelets and an increased transmission resistance. However, an equivalent circuit model employed for fitting of the EIS data results in Fig. 4e revealed that the carrier lifetime of the CBN platelets is longer. The carrier lifetime (τ) can be calculated according to the equation:

$$\tau = \frac{1}{2\pi f_{max}} \tag{4}$$

where f_{max} is the highest frequency in Nyquist plots as shown in Fig. 4e. The electron lifetimes are 50.37 ms to 41.55 ms for the CBN platelets and CBN particles, respectively. The lower resistance suggests that charges could not easily gather on the CBN platelet, which implies a reduced resistance to charge transfer [37]. The charge dynamic behavior is further measured by time-resolved photoluminescence (PL) decay spectroscopy. As shown in Fig. 4f, both emission patterns follow one exponential decay for the CBN particles and CBN platelets. The decline of the PL lifetime of the CBN particles and platelets are 1.87 and 1.92 ns respectively,

according to Fig. 4f. The longer PL lifetime of the CBN platelets provide further evidence of more efficient suppression of detrimental charge recombination during progression of the catalytic process [38].

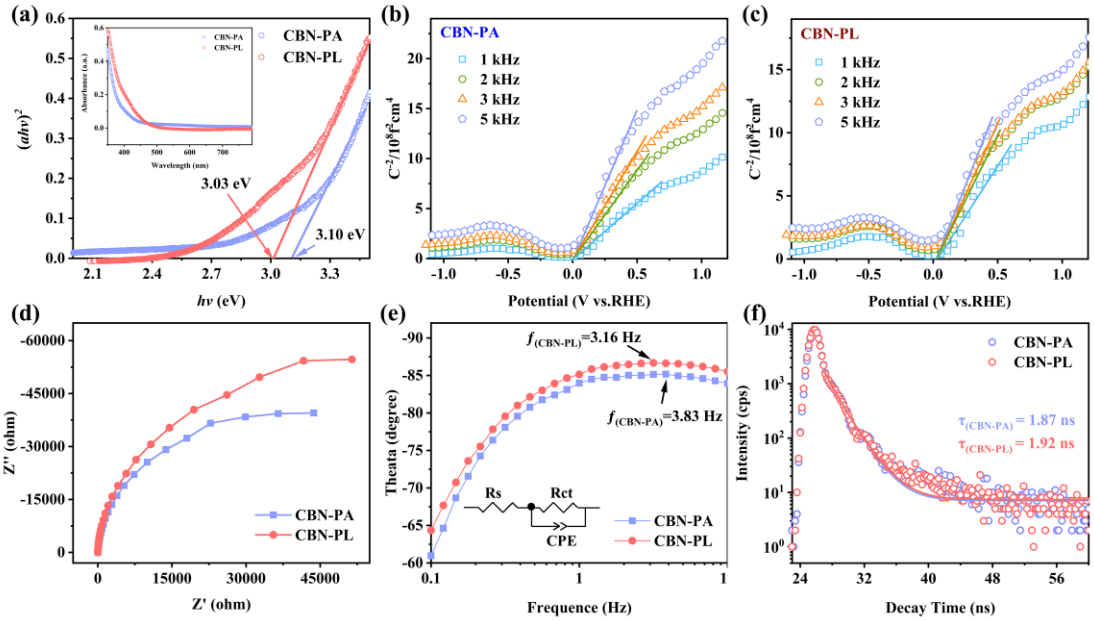

Fig. 4. (a) UV-vis diffuse reflectance spectra and the corresponding bandgap of $CaBi_2Nb_2O_9$ (CBN) particles and platelets. Mott-Schottky plots of (b) CBN particles and (c) CBN platelets at different frequencies. (d) EIS Nyquist plots, (e) Bode phase plots and (f) time-resolved PL decay spectra of CBN particles and platelets.

Fig. 5 shows the XPS spectra of the CBN particles and CBN platelets. The two signals in Fig. 5a show binding energies at approximately 164.2 eV and 158.9 eV, and correspond to those reported in the literature for Bi 4f [39]. The binding energies of Ca 2p (Fig. 5b) are located at 350.0 eV and 346.5 eV, indicating the A site atom of the $(CaNb_2O_7)^{2-}$ pseudo perovskite slabs has a stable chemical valence state [40]. The Nb 3d XPS measurements in Fig. 5c shows two signals at approximately 209.4 eV and 206.6 eV, which are attributed to the Nb 3d3/2 and Nb 3d5/2, and is associated with

the Nb element within +5 chemical state [41]. In addition, the wide peak in the O 1s spectrum (Fig. 5d) located at ~529.7 eV corresponds to the Nb-O bonds in the octahedral NbO_6, and the clear peak located at 532.6 eV belongs to the Bi-O bonds in the $(Bi_2O_2)^{2+}$ layer and a O-H, which is adsorbed at the surface [40, 41]. The shoulder peak near to Nb-O bonds at approximately 530.9 eV belongs to oxygen vacancies [42]. During the high temperature sintering process of the CBN samples, Bi_2O_3 is inevitably volatilized due to its lower melting point, resulting in oxygen vacancies of Nb produced for the electric equilibrium as in equations (1) and (2) [43].

$$2\,Bi^{\times} + 3O_O^{\times} \rightarrow 2\,V_{Bi}^{'''} + 3\,V_o^{\bullet\bullet} + Bi_2O_3 \uparrow \quad (1)$$

$$V_o^{\bullet\bullet} + 1/2\,O_2 \rightarrow O_O^{\times} + 2h^{\bullet} \quad (2)$$

The intensity of the shoulder peak for the oxygen vacancy (Ov) in the CBN platelet is lower than that of the CBN particle, see Fig. 5d; this indicates that more Bi_2O_3 in the CBN particles volatilizes and generates more vacancies, which is further verified by the test of oxygen vacancies in Electron Paramagnetic Resonance spectroscopy (EPR). The C 1s at 284.80 eV, as shown in Fig. 5e, is attributed to hydrocarbons generated by the XPS instrument and used for calibration of the binding energies. The survey scan in Fig. 5f indicates that there are no impurity elements such as Na, K, or Cl residues in the sample.

EPR is employed to verify the oxygen vacancies in the CBN particle and platelet, respectively. According to Fig. 5g, the Landé *g* factor peaks at 2.003, which demonstrates the presence of oxygen vacancies in both the CBN particle and CBN platelet lattices [44, 45]. In addition, the oxygen vacancy intensity of the CBN

particles is higher than that of the CBN platelets, which is consistent with the XPS results. The grains of CBN platelets are inclined to grow along the major planes (0010) facets preferentially, according to the XRD patterns shown in Fig. 5h. However, the grains of the CBN particles are inclined to preferentially grow along the (115) facets. Unlike the crystal growth diffusion mechanism in a traditional solid-state reaction, the mechanism of crystal growth in the molten salt method is interface controlled [46]. The major plane is destroyed owing to the difference in stress between the inside and on the surface of the grains in the liquid molten salt. The specific surface area of the CBN particle is 2.332 $m^2 \cdot g^{-1}$, which is 3.4 times higher than that of CBN platelets (0.695 $m^2 \cdot g^{-1}$), as shown in Fig. 5i. The SEM image spectra are illustrated in Fig. S1.

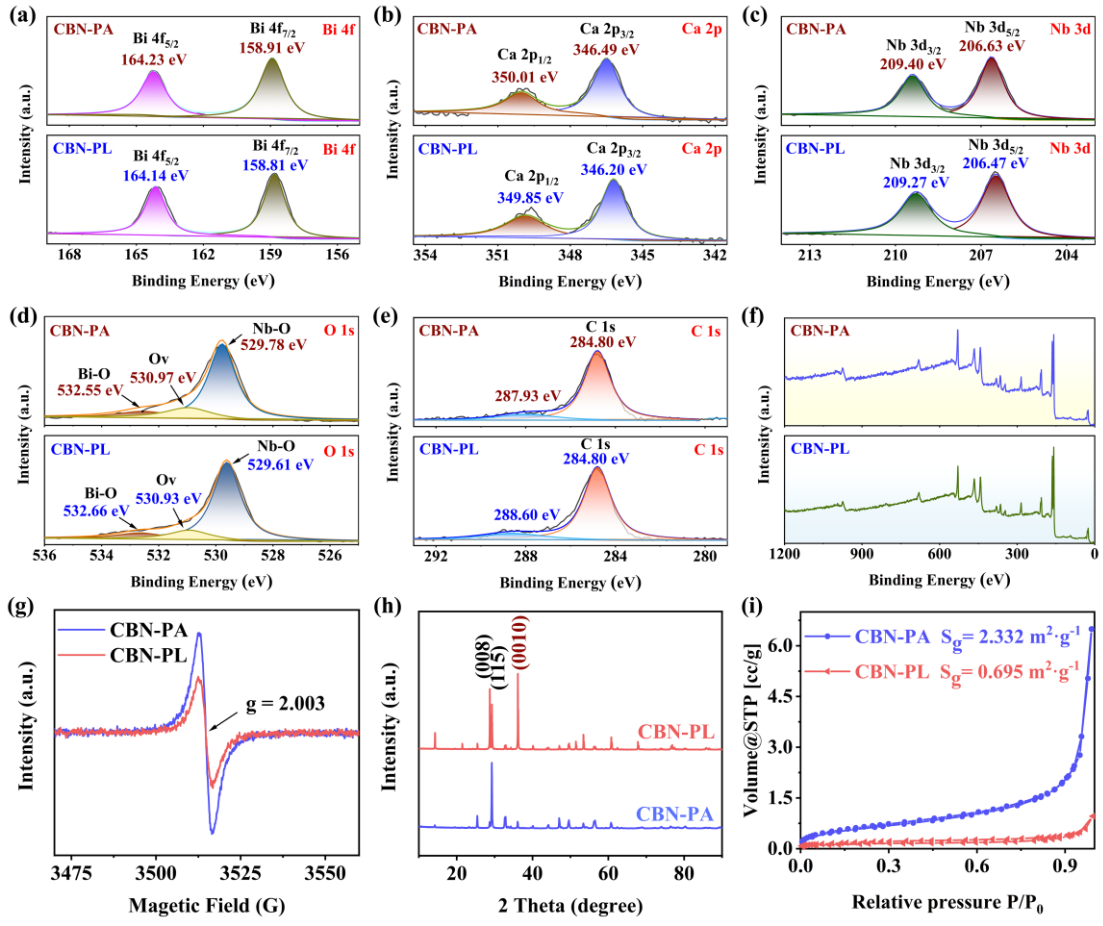

Fig. 5. XPS spectra of $CaBi_2Nb_2O_9$ (CBN) particle and platelet: (a) Bi 4f, (b) Ca 2p, (c) Nb 3d, (d) O 1s, (e) C 1s and (f) O 1s (f) survey; (g) EPR spectra, (h) XRD pattern, and (i) specific surface area of CBN particle and platelet.

3.2. Catalytic activity performance

After the above characterization and DFT analysis, we observed that the CBN platelets exhibit a better crystal structure and space arrangement of atoms, while the CBN particles show the advantages of a higher specific surface area and number of vacancies. Therefore, the piezocatalytic, photocatalytic and piezo-photocatalytic properties are investigated to verify which factors are dominant in the catalytic process, as shown in Fig. 6. Figs. 6a - 6c presents the degradation efficiency of both the CBN particles and CBN platelets, with simultaneous treatment by light (for photo-catalysis) and the application of ultrasound (for piezo-catalysis). The detailed UV-vis absorbance spectra are illustrated in Figs. S3-S4. The RhB degradation rate during piezo-photocatalysis of the CBN particles, CBN platelets, and with no CBN additive (as a control) are 98.7%, 96.7% and 25.8% in 32 min, 60 min and 60 min, which corresponds to a rate constant of 0.131 min^{-1}, 0.06 min^{-1} and 0.005 min^{-1}, respectively. This result demonstrated that pure CBN in both particle and platelet form exhibits excellent potential as a catalyst.

The piezo- (ultrasound only), photo- (light only), and piezo-photocatalytic (both light and ultrasound) performance of the CBN materials are shown in Figs. 6d - 6f. The dye degradation rate of the CBN particles under combined piezo-photocatalytic activation is 0.060 min^{-1}, which is much higher than that of photocatalytic alone

(0.029 min^{-1}) or piezocatalytic alone (0.009 min^{-1}); this implies that the combination of the application of ultrasound and light can achieve a significant enhancement in the surface charge of materials with both piezoelectric and optoelectronic properties. Furthermore, the degradation rate constant of CBN platelets reaches 0.066 min^{-1} and 0.026 min^{-1} under ultrasound only activation and when only stimulated by sunlight respectively, but reaches a higher value of 0.131 min^{-1} under the combination of both ultrasound and light, which exceeds the sum of the individual piezocatalytic and photocatalytic processes. The individual photocatalytic performance of both CBN samples of different dimensions is higher than their individual piezocatalytic performance, which suggests that photocatalysis plays a dominant role for a typical CBN piezoelectric material. Since CBN has a wide band gap, as in Fig. 4a, the utilization of visible light is limited. However, bismuth vacancies and oxygen vacancies are formed due to the easy volatilization of Bi_2O_3 during high temperature processing. The oxygen vacancies are able to generate a large number of holes during the cooling process, thereby forming a p-type conduction mechanism and reducing the resistivity. In addition, the $(Bi_2O_2)^{2+}$ layer is often used to replenish space charges and suppress the migration and aggregation of oxygen vacancies to domain walls. The $(Bi_2O_2)^{2+}$ layer, with its exposed facets (020) and (200) crystals, electron transport channels and low electron excitation energy can effectively promote carrier transport in the bulk phase and is beneficial to the photocatalytic performance. However, its weak piezoelectric catalytic performance is primarily limited by the low piezoelectric coefficient of CBN [47, 48]. In addition, this observation indicates that there is a

coupling of piezoelectric and photocatalytic effects for piezo-photocatalysis in CBN with dual piezoelectric and optoelectronic properties, and the piezoelectric field contributes to the separation of carriers, resulting in enhanced piezo-photocatalytic performance.

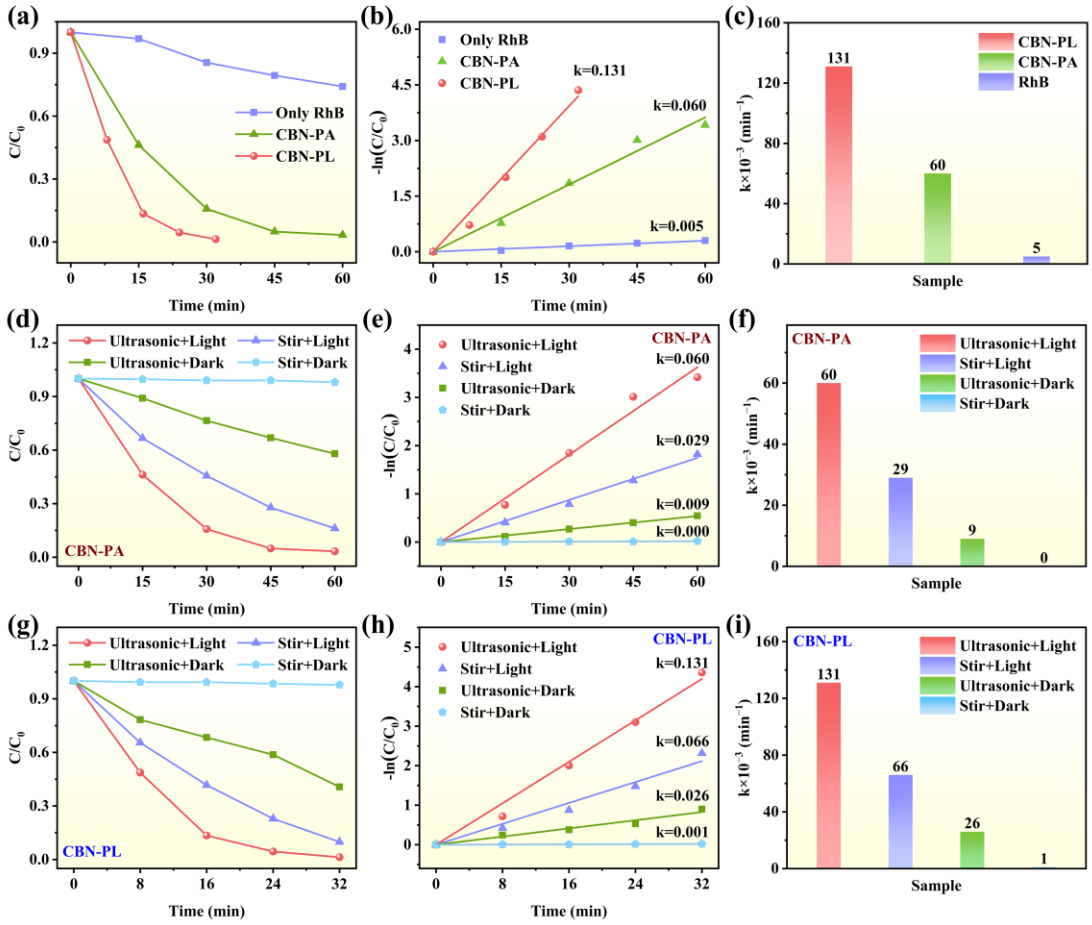

Fig. 6. (a) Piezo-photocatalytic degradation efficiencies of RhB as a function of time with $CaBi_2Nb_2O_9$ (CBN) particles or CBN platelets or no additives (as a control); corresponding (b) linear fitting of pseudo-first-order kinetics and (c) rate constant k values. (d) Piezo-, photo-, and piezo-photocatalytic performance of CBN particle and corresponding (e) kinetic curves and (f) rate constant k values. (g) Piezo-, photo-, and piezo-photocatalytic performances of CBN platelet and the corresponding (h) kinetic curves and (i) rate constant *k* values.

Several quenching experiments were performed to ascertain the active species involved in this piezo-Fenton process. Radical scavenger additives were added to explore the role of free radicals in the catalytic oxidation process. Phenylhydrazine (BQ), ethylenediamine tetraacetate dehydrate (EDTA) and tert-butyl alcohol (TBA) were selected as $\bullet O_2^-$, h^+ and •OH scavengers, respectively. As shown in Figs. 7a and Fig. S2, the degradation rate of RhB is decreased to only 48.5% at 32 min with the addition of BQ, corresponding to a rate constant of 0.025 min^{-1}. With the addition of EDTA, 87.2% of RhB is decomposed at 32 min where the rate constant is 0.064 min^{-1}. When TBA was added to the reaction system, the degradation ratio reaches 95.3% in 32 min, with a rate constant of 0.086 min^{-1}. The use of CBN platelets without any scavengers exhibits the highest pseudo-first-order reaction kinetics (k = 0.131 min^{-1}), as shown in Fig. 7a and Fig. S2b. These results indicate that abundant $\bullet O_2^-$ radicals are produced and act as a major free radical in the catalytic oxidation process. The h^+ and •OH radicals also play a role in the process of dye decomposition under ultrasonic agitation together with light irradiation. It is worth noting that these scavengers, especially for TBA molecules, are self-degraded under the combined effect of ultrasound and light irradiation. The DMSO-$\bullet O_2^-$ and DMPO-•OH signals are further confirmed by the electron paramagnetic resonance (EPR) testing, as shown in Figs. 7b-7c [49]. In Fig. 7b, a quartet peak with intensity ratio of 1:1:1:1 is demonstrated and there are cleat split peaks in the middle two peaks, which is in accordance with a typical pattern of the DMSO-$\bullet O_2^-$ signal. The four characteristic peaks with an intensity ratio of 1:2:2:1 belongs to the DMPO-•OH adducts, as shown in Fig. 7c. As

a result, $\bullet O_2^-$, h^+ and •OH scavengers are considered as the main reactive free radicals involved in the process of dye degradation, which can be assumed to proceed via the following equations:

$$CBN + vibration + irradiation \rightarrow CBN\ (h^+ + e^-) \quad (5)$$

$$O_2 + e^- \rightarrow \bullet O_2^- \quad (6)$$

$$\bullet O_2^- + e^- + 2H^+ \rightarrow H_2O_2 \quad (7)$$

$$H_2O_2 \rightarrow \bullet OH + \bullet OH \quad (8)$$

$$H_2O + h^+ \rightarrow \bullet OH + H^+ \quad (9)$$

According to the quenching experiments, the influence of the $\bullet O_2^-$ radicals are the most serious, and the decrease caused by •OH is higher than that of h^+ in the catalytic oxidation process. If the generation of •OH is shown as Eq. (9), which is independent of $\bullet O_2^-$, the piezo-photocatalytic degradation efficiency should be almost the same after the addition of EDTA and TBA. However, when the h^+ is trapped, its catalytic performance is higher than when the •OH is trapped, which suggests that there are other ways to generate the •OH, as shown in Eqs (7) and (8).

In Fig. 7d, the repeatability and stability of CBN platelets is investigated and present a similar degradation reaction rate across five runs, indicating that the CBN platelets maintain a high activity after cyclic experiments, which is important for its practical application. XRD scan patterns and SEM images of the surface of the CBN platelets after cyclic testing are shown in Fig. S5 and Fig. S6, respectively. This further verifies the high stability of the CBN platelets, where the structure and morphology of the platelets were almost unchanged after repeated use. Fig. 7e shown a comprehensive comparison of previously reported piezo-photocatalysts for degradation of RhB for

intrinsic systems based on a single material and composite systems, where the results indicate that the catalytic activity of the CBN platelets is highly promising as a coupled piezo-photocatalytic material [50-61].

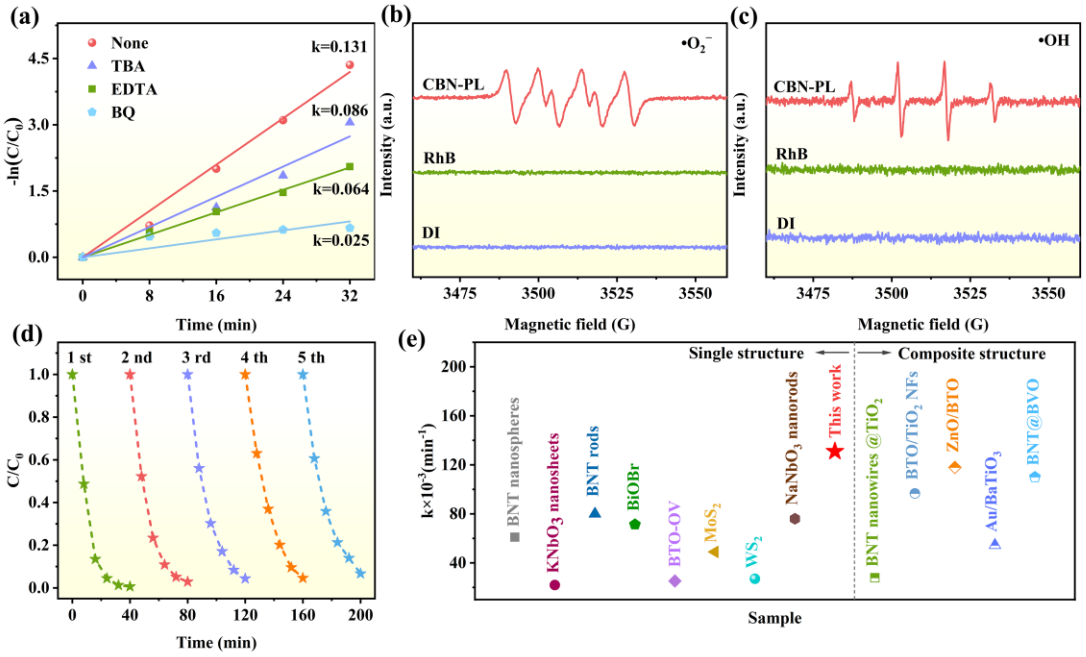

Fig. 7. (a) Kinetic curves of $CaBi_2Nb_2O_9$ (CBN) platelet with the addition of scavengers for the degradation of RhB. ESR signals for (b) DMPO/DMSO-•O_2^- and (c) DMPO-•OH under simultaneous light and ultrasonic irradiation. (d) Consecutive cycling catalytic performances of CBN platelet toward bleaching of RhB. (e) Comprehensive comparison of previously reported piezo-photocatalysts for degradation of RhB.

3.3 Analysis of mechanism of catalysis

The piezoelectric properties of CBN platelet is characterized by piezoresponse force microscopy (PFM). As illustrated in Figs. 8a-8b, the CBN platelet exhibits a surface potential of ≈ 60 mV, and the topographic AFM image shown in Fig. 8c and Fig. 8d reveals that the thickness of a CBN platelet is approximately 620 nm. The

piezoresponse of a CBN platelet is illustrated in Fig. 8e, where the applied tip bias sweeps from −12 V to +12 V, and the deformation of the CBN platelet is generated by the converse piezoelectric effect caused by the direct current (DC) bias. The variation in piezo-response amplitude with tip bias voltage shows a typical “butterfly loop” shape, and is in agreement to the strain-electric field (*S* - *E*) curve of piezoelectric materials. Under an opposite tip bias, there is a phase reversal of ~180 ° in the CBN platelets, as shown in Fig. 8f. Theoretically, the phase-shift response of the PFM with respect to the alternating current (AC) voltage corresponds to the domain orientation: the attractive forces by negative polar surface shifts phase negatively, while the repulsive forces by the positive polar surface shift phase positively [62]. The phase reversal demonstrated in the piezoresponse phase-voltage hysteresis loop in Fig. 8e indicates the existence of 180 ° domain switching process. The clear PFM amplitude butterfly loops and phase hysteresis loops further verify the non-zero remnant polarization of the CBN platelets.

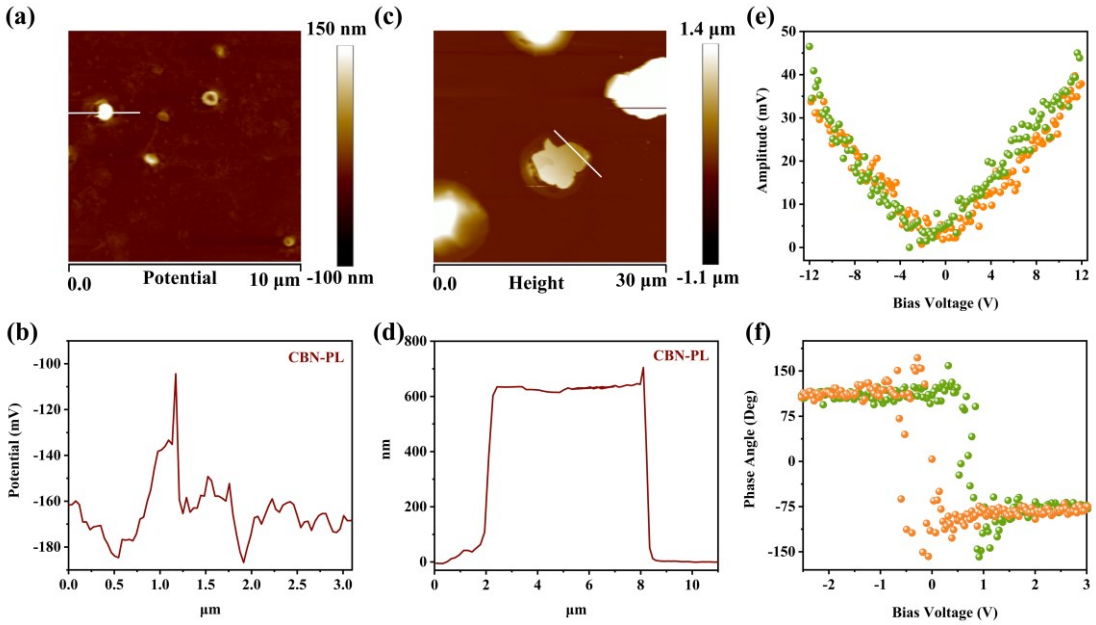

Fig. 8. PFM of the $CaBi_2Nb_2O_9$ (CBN) platelet, (a) relative amplitude of piezoelectric response, (b) corresponding profile of electrical output (mV) as a function of distance, (c) topographic image, (d) corresponding height profile of morphology image, (e) PFM amplitude butterfly loops and (f) PFM phase hysteresis loops of CBN platelet.

A COMSOL multi-physics simulation is now employed to explore the correlation between CBN morphology and piezoelectric potential. During the simulation process, we found that for different fixed points, the deformation of the material is different, and the magnitude of the generated electric potential is therefore changed. The dimensions of the simulation were consistent with material dimensions obtained by electron microscopy, where the diameter of the simulated CBN particle is 500 nm, and the size of the simulated CBN platelet is 10 um ×10 um × 0.4 um. In addition, the applied stress is set as 1.0×10^8 Pa, which is typical of the stress induced by ultrasound [63, 64]. As shown in Fig. 9a, the piezoelectric potential difference across the CBN particle is 2.64 V for a symmetrical stress distribution applied to the whole surface of CBN particle with the center fixed. However, the piezoelectric potential across a CBN platelet is 3.05 V (Fig. 9c) for a fixed center point.

Since bubble cavitation during the application of ultrasound is unlikely to be symmetrical on the surface of the material, we simplified the model to a stress that is applied on one side. Fig. 9b and Fig. 9d show that the piezoelectric potential of the CBN particle is 2.90 V for a fixed bottom and the applied stress on the top hemi-particle. For the CBN platelet, when the center point of the platelet was fixed and a stress was applied to the top of the platelet, as shown in the Fig. 9d, the

piezoelectric potential was 3.38 V. In addition, Fig. S7 shows data when the center of the CBN particle and CBN platelet were fixed, with an applied force on the top hemi-particle and top plate surface, respectively. When the volume of the central fixed region of material increases, the electrical potential generated by the material decreases. When the applied force is transmitted to the central fixed region, a smaller fixed region leads to a greater stress (force per unit area), and a higher level of local deformation. As a result, the calculated potential will be higher and in Fig. S7 fixed central positions of different sizes are designed with equal proportions for the two geometries, where the simulations show that the electric potential generated by a CBN platelet is higher than that generated by a CBN particle for all cases. This, combined with the large piezo-potential generated from a surface stress, also verifies that the piezo-catalytic performance of the CBN platelet is higher than that of the CBN particle.

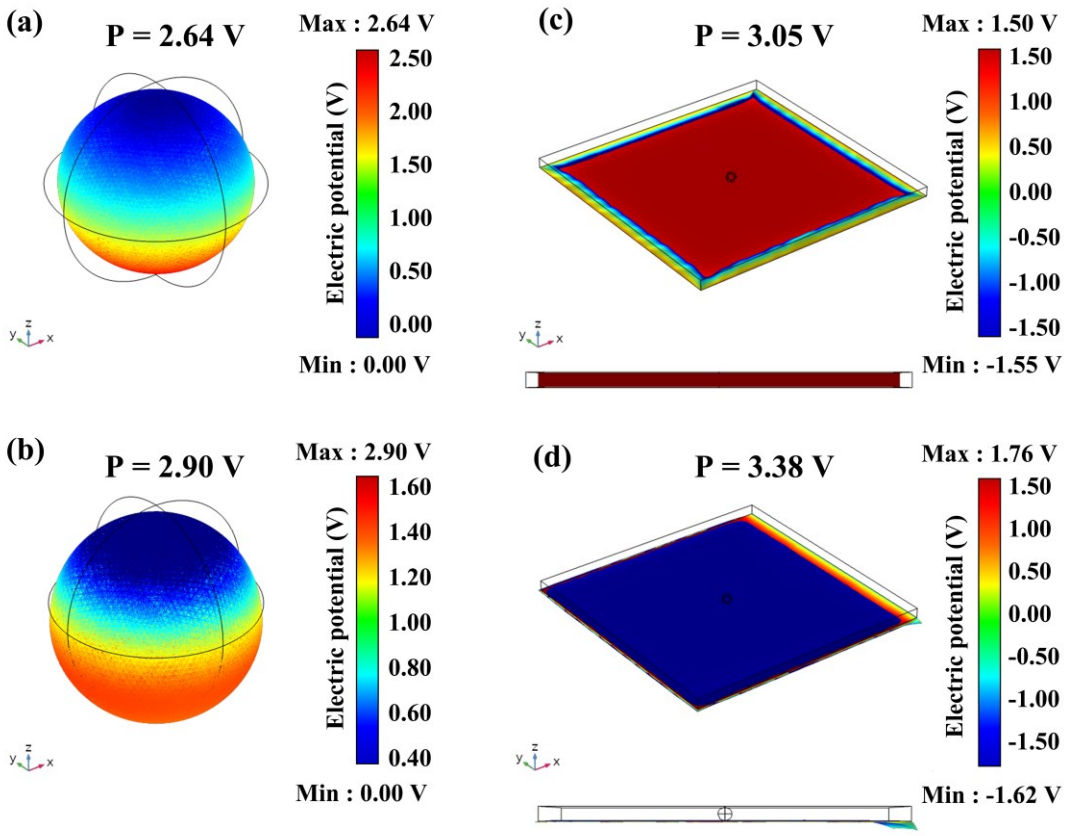

Fig. 9. Theoretical analysis of the piezo-potential distribution according to the volumetric stress distribution. $CaBi_2Nb_2O_9$ (CBN) particle with (a) center point fixed and force applied to all points on the surface of the particle; (b) bottom fixed and applied force to the top hemi-particle; CBN platelet with (c) center point fixed and force on the all the surface, and (d) bottom fixed and force on the upper surface.

Since the CBN platelets exhibit the best catalytic characteristics, their use for water splitting for H_2 production through the photo-, piezo-, and piezo-phototronic effects are further investigated in detail in Fig. 10a. The photocatalytic activity of the CBN platelets is approximately 29.60 $\mu mol \cdot g^{-1} \cdot h^{-1}$, while the piezo-catalytic activity is higher at 72.12 $\mu mol \cdot g^{-1} \cdot h^{-1}$. Crucially, through the combined piezo-photocatalytic process, a significant improvement is observed and the generated H_2-production rate reached approximately 96.83 $\mu mol \cdot g^{-1} \cdot h^{-1}$. This result is in good agreement with our

dye degradation test, where a synergistic piezo-photocatalytic effect is observed and the piezoelectric field generated in the CBN platelets can effectively inhibit the recombination of photogenerated carriers. After undertaking piezo-photocatalysis for hydrogen production, there is no change of the morphology structure of the CBN platelet, which is shown in Fig. S8. Fig. 10b shows the crystal structure of the CBN platelet, where CBN is a typical Aurivillius phase structure that consists of alternating layers of bismuth oxide $(Bi_2O_2)^{2+}$ and perovskite-like layers $(CaNb_2O_7)^{2-}$. Due to its unique 2D layered structure, the spontaneous polarization is confined to the a-b plane.

The basic principle of piezo-enhanced photocatalysis is shown in Figs. 10c-10d. When CBN is only exposed to light, due to its wide band gap, the utilization of light is limited and electrons and holes readily recombine in the bulk and surface during their transport to the surface of the material. The regular bismuth layer structure reduces the electron transmission resistance, and its photoelectric conversion efficiency is limited. Under the action of dark-state ultrasound, the CBN platelets has a certain efficiency for dye degradation and hydrogen production, which indicates that the positive and negative charges generated on the surface after ultrasonic deformation can also participate in the catalytic reaction. The perovskite-like layers $(CaNb_2O_7)^{2-}$ with a non-centrosymmetric structure is deformed when subject to mechanical vibrations, such as ultrasound, and the thin CBN platelet are readily bent to generate positive and negative charges on the surface of CBN platelet. In conclusion, the reasons for $CaBi_2Nb_2O_9$ platelets exhibiting excellent piezo-photocatalytic performance can be attributed to the following aspects: (i) the

surface of the CBN platelets attracts a large amount of dissociated hydrogen and hydroxide ions due to the dominating active exposing facets of the (020) and (200) crystal planes of the CBN platelet; (ii) inside the CBN platelet, the electron transport channels in the (200) crystal plane have a lower energy for electron excitation, and (iii) the generated built-in electric field under the application of ultrasound can greatly inhibit the recombination of photogenerated carriers.

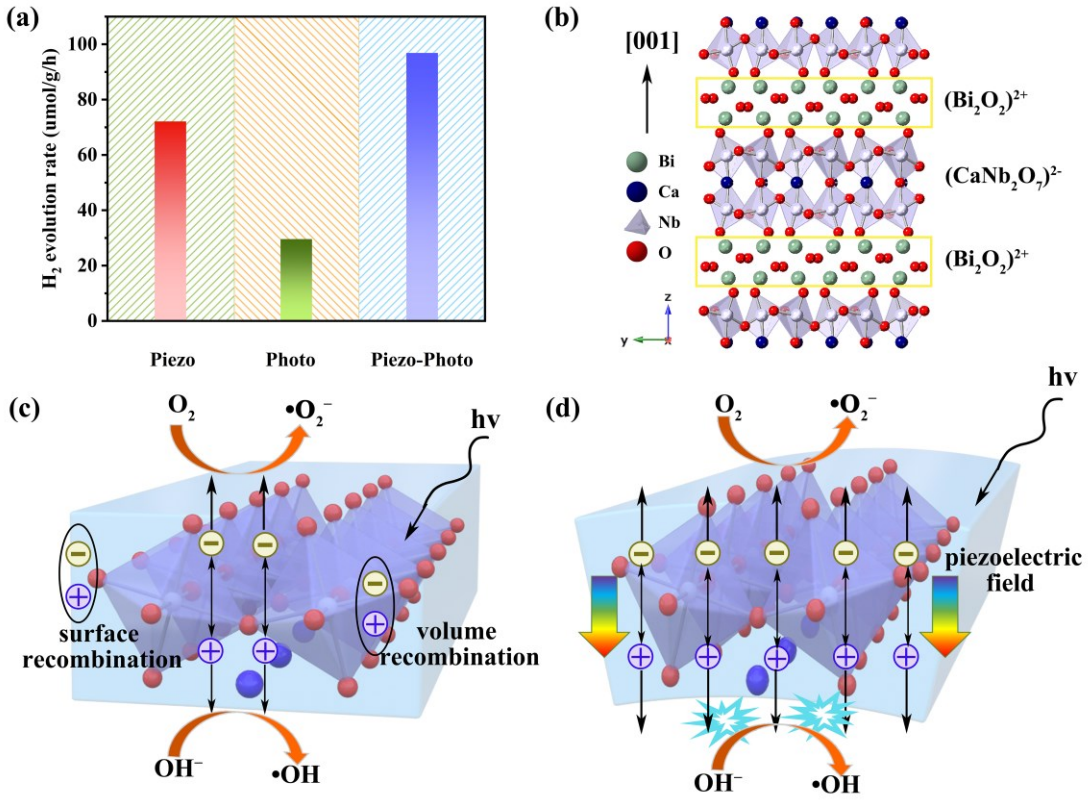

Fig. 10 (a) Piezo-, photo- and piezo-photocatalytic hydrogen production from water splitting by a $CaBi_2Nb_2O_9$ (CBN) platelet, (b) crystal structure of CBN platelet, schematic representation of transfer processes of photoexcited charge carriers (c) without and (d) with mechanical vibration.

4. Conclusions

This paper has examined the unique piezo-catalytic and photo-catalytic properties of

$CaBi_2Nb_2O_9$ platelets that contain structured $(Bi_2O_2)^{2+}$ layers, which were synthesized via a molten salt method. To explore the influence of $CaBi_2Nb_2O_9$ morphology on catalytic performance, an in-depth analysis of the materials included phase analysis, electron microscopy, UV-Vis spectroscopy, and catalytic performance. Detailed atomistic modelling was further employed to gain new insights on the differences between the different crystal planes of the $CaBi_2Nb_2O_9$. It was demonstrated that while the $CaBi_2Nb_2O_9$ platelets have a smaller specific surface area and fewer oxygen vacancies than the $CaBi_2Nb_2O_9$ particles, the unique bismuth layer structure of the platelets provides active exposed facets on the (020) and (200) planes, thereby producing high electron transport channels and a low electron excitation energy. These attractive features effectively promote carrier transport in the bulk phase to achieve an enhanced catalysis performance. In addition, the thinner plate-like structure is easier to deform under the application of ultrasound, leading to a larger piezoelectric field to inhibit the recombination of carriers.

For water splitting applications, the $CaBi_2Nb_2O_9$ platelets exhibit a high hydrogen yield rate of 96.83 $\mu mol \bullet g^{-1} \bullet h^{-1}$ under the combined action of irradiation by light and ultrasound, without the need to use a sacrificial agent. For water treatment applications, the piezo-photocatalytic decomposition ratio for a Rhodamine B (RhB) dye can be up to 98.7% in only 32 min using the $CaBi_2Nb_2O_9$ platelets, with a high rate constant of k = 0.131 min^{-1}. As a result, this work demonstrates the unique potential of $CaBi_2Nb_2O_9$ platelets with structured $(Bi_2O_2)^{2+}$ layers in terms of providing excellent piezo-photocatalytic performance for applications related to water

splitting and water treatment. This work therefore provides a new approach for the design and manufacture advanced materials with enhanced photocatalytic performance by exploiting structured layers to couple piezo- and photo-catalytic effects

Acknowledgement

This work was financially supported by Hunan Excellent Youth Science Foundation (2022JJ20067), Scientific research project of Hunan Provincial Department of Education (21B0009), the National Natural Science Foundation of China (52002404, 52172265), Construction of Innovative Provinces in Hunan Province of China (No. 2020GK2062), Student innovation Project of Central South University (No. S2022105330581) and the State Key Laboratory of Powder Metallurgy, Central South University, Changsha, China.

Conflict of interest

The authors declare no conflict of interest.

References

[1] H. Xue, H. Gong, Y. Yamauchi, T. Sasaki, R. Ma. Photo-enhanced rechargeable high-energy-density metal batteries for solar energy conversion and storage. Nano Research Energy. 2022;1.

[2] F. Liu, M. Wang, X. Liu, B. Wang, C. Li, C. Liu, et al. A rapid and robust light-and-solution-triggered in situ crafting of organic passivating membrane over metal halide perovskites for markedly improved stability and photocatalysis. Nano Lett. 2021;21(4):1643-50.

[3] B. Dai, G.M. Biesold, M. Zhang, H. Zou, Y. Ding, Z.L. Wang, et al. Piezo-phototronic effect on photocatalysis, solar cells, photodetectors and light-emitting diodes. Chem Soc Rev. 2021;50(24):13646-91.

[4] Y.J. Chung, C.S. Yang, J.T. Lee, G.H. Wu, J.M. Wu. Coupling effect of piezo-flexocatalytic hydrogen evolution with hybrid 1T- and 2H-phase few-layered $MoSe_2$ nanosheets. Adv Energy Mater. 2020;10(42):2002082.

[5] C. Hu, F. Chen, Y. Wang, N. Tian, T. Ma, Y. Zhang, et al. Exceptional cocatalyst-free photo-enhanced piezocatalytic hydrogen evolution of carbon nitride nanosheets from strong in-plane polarization. Adv Mater. 2021;33(24):9.

[6] L. Chen, S. Li, Z. Yang, C. Chen, C. Chu, B. Chen. Enhanced photocatalytic hydrogen peroxide production at a solid-liquid-air interface via microenvironment engineering. Appl Catal B. 2022;305:121066.

[7] M. Wang, Y. Zuo, J. Wang, Y. Wang, X. Shen, B. Qiu, et al. Remarkably enhanced hydrogen generation of organolead halide perovskites via piezocatalysis and photocatalysis. Adv Energy Mater. 2019;9(37):1901801.

[8] B. Dai, J. Fang, Y. Yu, M. Sun, H. Huang, C. Lu, et al. Construction of infrared-light-responsive photoinduced carriers driver for enhanced photocatalytic hydrogen evolution. Adv Mater. 2020;32(12):e1906361.

[9] S. Xu, W. Qian, D. Zhang, X. Zhao, X. Zhang, C. Li, et al. A coupled photo-piezo-catalytic effect in a BST-PDMS porous foam for enhanced dye wastewater degradation. Nano Energy. 2020;77:105305.

[10] Q. Liu, Z. Li, J. Li, F. Zhan, D. Zhai, Q. Sun, et al. Three dimensional $BaTiO_3$

piezoelectric ceramics coated with TiO_2 nanoarray for high performance of piezo-photoelectric catalysis. Nano Energy. 2022;98:107267.

[11] Q. Liu, D. Zhai, Z. Xiao, C. Tang, Q. Sun, C.R. Bowen, et al. Piezo-photoelectronic coupling effect of $BaTiO_3$@TiO_2 nanowires for highly concentrated dye degradation. Nano Energy. 2022;92:106702.

[12] B. Dai, Y. Yu, Y. Chen, H. Huang, C. Lu, J. Kou, et al. Construction of self-healing internal electric field for sustainably enhanced photocatalysis. Adv Funct Mater. 2019;29(16):1807934.

[13] Q. Xu, X. Gao, S. Zhao, Y.-N. Liu, D. Zhang, K. Zhou, et al. Construction of bio-piezoelectric platforms: from structures and synthesis to applications. Adv Mater. 2021;33(27):e2008452.

[14] Y. Kang, L. Lei, C. Zhu, H. Zhang, L. Mei, X. Ji. Piezo-photocatalytic effect mediating reactive oxygen species burst for cancer catalytic therapy. Materials Horizons. 2021;8(8):2273-85.

[15] S. Liang, X. Deng, P.a. Ma, Z. Cheng, J. Lin. Recent advances in nanomaterial-assisted combinational sonodynamic cancer therapy. Adv Mater. 2020;32(47):e2003214.

[16] Y. Wang, X. Wen, Y. Jia, M. Huang, F. Wang, X. Zhang, et al. Piezo-catalysis for nondestructive tooth whitening. Nat Commun. 2020;11(1):1-11.

[17] D. Zhang, H. Wu, C.R. Bowen, Y. Yang. Recent advances in pyroelectric materials and applications. Small. 2021:e2103960.

[18] X. Yu, S. Wang, X.D. Zhang, A.h. Qi, X.R. Qiao, Z.R. Liu, et al.

Heterostructured nanorod array with piezophototronic and plasmonic effect for photodynamic bacteria killing and wound healing. Nano Energy. 2018;46:29-38.

[19] B. Dai, H. Feng, Z. Li, Y. Xie. Field enhanced photocatalytic disinfection. Sci Bull (Beijing). 2022;67(8):779-83.

[20] B. Dai, Y. Zhou, X. Xiao, Y. Chen, J. Guo, C. Gao, et al. Fluid field modulation in mass transfer for efficient photocatalysis. Advanced Science. 2022;9(28):e2203057.

[21] S. Tu, Y. Zhang, A.H. Reshak, S. Auluck, L. Ye, X. Han, et al. Ferroelectric polarization promoted bulk charge separation for highly efficient CO_2 photoreduction of $SrBi_4Ti_4O_{15}$. Nano Energy. 2019;56:840-50.

[22] J. Gu, Y. Peng, T. Zhou, J. Ma, H. Pang, Y. Yamauchi. Porphyrin-based framework materials for energy conversion. Nano Research Energy. 2022;1.

[23] C. Hu, H. Huang, F. Chen, Y. Zhang, H. Yu, T. Ma. Coupling piezocatalysis and photocatalysis in Bi_4NbO_8X (X = Cl, Br) polar single crystals. Adv Funct Mater. 2019;30(7).

[24] X. Zhou, F. Yan, S. Wu, B. Shen, H. Zeng, J. Zhai. Remarkable piezophoto coupling catalysis behavior of $BiO_X/BaTiO_3$ (X = Cl, Br, $Cl_{0.166}$ $Br_{0.834}$) piezoelectric composites. Small. 2020;16(26):2001573.

[25] W. Hou, Z. Chen, L. Liu. Strong synergy of piezoelectric photocatalysis in PFC catalyzed by BaTiO3/Bi2WO6 anode and with peroxymonosulfate to remove rhodamine B. J Sol-Gel Sci Technol. 2022;104(1):125-37.

[26] Y. Li, Y. Zhao, G. Wu, H. Ma, J. Zhao. Bi superlattice nanopolygons at BiOCl (001) nanosheet assembled architectures for visible-light photocatalysis. Mater Res

Bull. 2018;101:39-47.

[27] H. Suzuki, M. Higashi, O. Tomita, Y. Ishii, T. Yamamoto, D. Kato, et al. $PbBi_3O_4X_3$ (X = Cl, Br) with single/double halogen layers as a photocatalyst for visible-light-driven water splitting: Impact of a halogen layer on the band structure and stability. Chem Mater. 2021;33(24):9580-7.

[28] S. Wei, Y. Chen, P. Wu, X. Liu, J. Ren, B. Yao, et al. Surface defects engineered $Bi_4Ti_3O_{12}$ nanosheets for photocatalytic degradation of antibiotic levofloxacin. Applied Catalysis A: General. 2022;640:118675.

[29] L. Jiang, J. Li, Y. Li, X. Wu, G. Zhang. Promoted charge separation from nickel intervening in $[Bi_2O_2]^{2+}$ layers of Bi_2O_2S crystals for enhanced photocatalytic CO_2 conversion. Appl Catal B. 2021;294:120249.

[30] H. Huang, Y. He, X. Li, M. Li, C. Zeng, F. Dong, et al. $Bi_2O_2(OH)(NO_3)$ as a desirable $[Bi_2O_2]^{2+}$ layered photocatalyst: strong intrinsic polarity, rational band structure and {001} active facets co-beneficial for robust photooxidation capability. J Mater Chem A. 2015;3(48):24547-56.

[31] Y. Zhang, J. Yuan, H. Gong, Y. Cao, K. Liu, H. Cao, et al. (001)-facet-exposed planelike $ABi_2Nb_2O_9$ (A = Ca, Sr, Ba) powders with a single-crystal grain for enhancement of photocatalytic activity. ACS sustainable chem eng. 2018;6(3):3840-52.

[32] Y. Li, G. Chen, H. Zhang, Z. Lv. Band structure and photocatalytic activities for H_2 production of $ABi_2Nb_2O_9$ (A = Ca, Sr, Ba). Int J Hydrogen Energy. 2010;35(7):2652-6.

[33] Q. Zhu, A.A. Dar, Y. Zhou, K. Zhang, J. Qin, B. Pan, et al. Oxygen vacancies promoted piezoelectricity toward piezo-photocatalytic decomposition of tetracycline over $SrBi_4Ti_4O_{15}$. ACS ES&T Engineering. 2022;2(8):1365-75.

[34] C. Yuan, Y. Shen, C. Zhu, P. Zhu, F. Yang, J. Liu, et al. Ru single-atom decorated black TiO_2 nanosheets for efficient solar-driven hydrogen production. ACS sustainable chem eng. 2022;10(31):10311-7.

[35] X. Zhang, P. Tang, G. Zhai, X. Lin, Q. Zhang, J. Chen, et al. Regulating phase junction and oxygen vacancies of TiO_2 nanoarrays for boosted photoelectrochemical water oxidation. Chemical Research in Chinese Universities. 2022;38(5):1292-300.

[36] J. Song, M.Z. Bazant. Effects of nanoparticle geometry and size distribution on diffusion impedance of battery electrodes. J Electrochem Soc. 2013;160(1):A15-A24.

[37] Hongtao Yuan, Hidekazu Shimotani, Jianting Ye, Sungjae Yoon, Hasniah Aliah, Atsushi Tsukazaki, et al. Electrostatic and electrochemical nature of liquid-gated electric-double-layer transistors based on oxide semiconductors. Journal of the American Chemical Society. 2010;132(51):18402−7.

[38] Y. Xi, Y. Zhang, X. Cai, Z. Fan, K. Wang, W. Dong, et al. PtCu thickness-modulated interfacial charge transfer and surface reactivity in stacked graphene/Pd@PtCu heterostructures for highly efficient visible-light reduction of CO_2 to CH_4. Appl Catal B. 2022;305:121069.

[39] A. Chauhan, H. Singh Kushwaha, R.V. Kumar, R. Vaish. $Bi_{0.5}Na_{0.5}TiO_3$-BiOCl composite photocatalyst for efficient visible light degradation of dissolved organic impurities. J Environ Chem Eng. 2019;7(1):102842.

[40] G. Liu, D. Wang, C. Wu, J. Wu, Q. Chen. A realization of excellent piezoelectricity and good thermal stability in $CaBi_2Nb_2O_9$: Pseudo phase boundary. J Am Ceram Soc. 2019;102(4):1794-804.

[41] A. Zhang, Z.Y. Liu, B. Xie, J.S. Lu, K. Guo, S.M. Ke, et al. Vibration catalysis of eco-friendly $Na_{0.5}K_{0.5}NbO_3$-based piezoelectric: An efficient phase boundary catalyst. Appl Catal B. 2020;279:119353.

[42] F. Zhan, Y. Liu, K. Wang, Y. Liu, X. Yang, Y. Yang, et al. In situ formation of WO(3)-based heterojunction photoanodes with abundant oxygen vacancies via a novel microbattery method. ACS Appl Mater Interfaces. 2019;11(17):15467-77.

[43] J. Robertson, C.W. Chen, W.L. Warren, C.D. Gutleben. Electronic structure of the ferroelectric layered perovskite $SrBi_2Ta_2O_9$. Appl Phys Lett. 1996;69(12):1704-6.

[44] Y. Chen, X. Deng, J. Wen, J. Zhu, Z. Bian. Piezo-promoted the generation of reactive oxygen species and the photodegradation of organic pollutants. Appl Catal B. 2019;258:118024.

[45] J. Hu, Y. Lu, X.-L. Liu, C. Janiak, W. Geng, S.-M. Wu, et al. Photoinduced terminal fluorine and Ti^{3+} in $TiOF_2/TiO_2$ heterostructure for enhanced charge transfer. CCS Chemistry. 2020;2(6):1573-81.

[46] J. Cahn. On the morphology stability of growth crystals. Crystal Growth: Pergamon Oxford, UK; 1967. p. 681.

[47] Z.-Y. Shen, C. Qin, W.-Q. Luo, F. Song, Z. Wang, Y. Li, et al. Ce and W co-doped CaBi2Nb2O9 with enhanced piezoelectric constant and electrical resistivity at high temperature. Journal of Materiomics. 2020;6(3):459-66.

[48] X. Xie, Z. Zhou, T. Chen, R. Liang, X. Dong. Enhanced electrical properties of NaBi modified CaBi2Nb2O9-based Aurivillius piezoceramics via structural distortion. Ceram Int. 2019;45(5):5425-30.

[49] H. Huang, S. Tu, C. Zeng, T. Zhang, A.H. Reshak, Y. Zhang. Macroscopic polarization enhancement promoting photo- and piezoelectric-induced charge separation and molecular oxygen activation. Angew Chem Int Ed Engl. 2017;56(39):11860-4.

[50] S. Li, Z. Zhao, D. Yu, J.-Z. Zhao, Y. Su, Y. Liu, et al. Few-layer transition metal dichalcogenides (MoS_2, WS_2, and WSe_2) for water splitting and degradation of organic pollutants: Understanding the piezocatalytic effect. Nano Energy. 2019;66:104083.

[51] A. Sharma, U. Bhardwaj, D. Jain, H.S. Kushwaha. $NaNbO_3$ nanorods: photopiezocatalysts for elevated bacterial disinfection and wastewater treatment. ACS Omega. 2022;7(9):7595-605.

[52] Q. Liu, Q. Hu, D. Zhai, Q.W. Sun, H. Luo, D. Zhang. Superior photo-piezoelectric catalytic performance using $Bi_{0.5}Na_{0.5}TiO_3$@$BiVO_4$ based cloth. J Mater Chem A. 2021;9:17841-54.

[53] P. Wang, X. Li, S. Fan, X. Chen, M. Qin, D. Long, et al. Impact of oxygen vacancy occupancy on piezo-catalytic activity of $BaTiO_3$ nanobelt. Appl Catal B. 2020;279:119340.

[54] C. Chao, Y. Zhou, T. Han, Y. Yang, J. Wei, H. Li, et al. Ferroelectric polarization-enhanced photocatalytic properties and photo-induced charge carrier

behavior of Au/$BaTiO_3$. J Alloys Compd. 2020;825:154060.

[55] Z. Liu, K. Zhao, G. Xing, W. Zheng, Y. Tang. One-step synthesis of unique thorn-like $BaTiO_3$-TiO_2 composite nanofibers to enhance piezo-photocatalysis performance. Ceram Int. 2021;47(5):7278-84.

[56] X.F. Zhou, Q.W. Sun, D. Zhai, G.L. Xue, H. Luo, D. Zhang. Excellent catalytic performance of molten-salt-synthesized $Bi_{0.5}Na_{0.5}TiO_3$ nanorods by the piezo-phototronic coupling effect. Nano Energy. 2021;84:105936.

[57] X.F. Zhou, S.H. Wu, C.B. Li, F. Yan, H.R. Bai, B. Shen, et al. Piezophototronic effect in enhancing charge carrier separation and transfer in ZnO/$BaTiO_3$ heterostructures for high-efficiency catalytic oxidation. Nano Energy. 2019;66:104127.

[58] X.G. Xu, X.J. Lin, F.H. Yang, S.F. Huang, X. Cheng. Piezo-photocatalytic activity of $Bi_{0.5}Na_{0.5}TiO_3$@TiO_2 composite catalyst with heterojunction for degradation of organic dye molecule. The Journal of Physical Chemistry C. 2020;124(44):24126-34.

[59] H. Lei, H. Zhang, Y. Zou, X. Dong, Y. Jia, F. Wang. Synergetic photocatalysis/piezocatalysis of bismuth oxybromide for degradation of organic pollutants. J Alloys Compd. 2019;809:151840.

[60] Z.C. Zhao, L.Y. Wei, S. Li, L.F. Zhu, Y.P. Su, Y. Liu, et al. Exclusive enhancement of catalytic activity in $Bi_{0.5}Na_{0.5}TiO_3$ nanostructures: new insights into the design of efficient piezocatalysts and piezo-photocatalysts. J Mater Chem A. 2020;8(32):16238-45.

[61] D.F. Yu, Z.H. Liu, J.M. Zhang, S. Li, Z.C. Zhao, L.F. Zhu, et al. Enhanced catalytic performance by multi-field coupling in $KNbO_3$ nanostructures: Piezo-photocatalytic and ferro-photoelectrochemical effects. Nano Energy. 2019;58:695-705.

[62] J. Wu, N. Qin, E. Lin, B. Yuan, Z. Kang, D. Bao. Synthesis of $Bi_4Ti_3O_{12}$ decussated nanoplates with enhanced piezocatalytic activity. Nanoscale. 2019;11(44):21128-36.

[63] J. Wu, N. Qin, D.H. Bao. Effective enhancement of piezocatalytic activity of $BaTiO_3$ nanowires under ultrasonic vibration. Nano Energy. 2018;45:44-51.

[64] S.C. Tu, Y.X. Guo, Y.H. Zhang, C. Hu, T.R. Zhang, T.Y. Ma, et al. Piezocatalysis and piezo-photocatalysis: catalysts classification and modification strategy, reaction mechanism, and practical application. Adv Funct Mater. 2020;30(48):2005158.